The Astrophysical Journal, 819:5 (15pp), 2016 March 1 doi:10.3847/0004-637X/819/1/5
© 2016. The American Astronomical Society. All rights reserved.

RAPIDLY RISING TRANSIENTS FROM THE SUBARU HYPER SUPRIME-CAM TRANSIENT SURVEY*

Masaomi Tanaka[1,2], Nozomu Tominaga[2,3], Tomoki Morokuma[2,4], Naoki Yasuda[2], Hisanori Furusawa[1], Petr V. Baklanov[5,6,7], Sergei I. Blinnikov[2,5,8], Takashi J. Moriya[9], Mamoru Doi[2,4], Ji-an Jiang[4], Takahiro Kato[10], Yuki Kikuchi[4], Hanindyo Kuncarayakti[11,12], Tohru Nagao[13], Ken'ichi Nomoto[2,14], and Yuki Taniguchi[4]

[1] National Astronomical Observatory of Japan, Mitaka, Tokyo 181-8588, Japan; masaomi.tanaka@nao.ac.jp
[2] Kavli Institute for the Physics and Mathematics of the Universe (WPI), The University of Tokyo, Kashiwa, Chiba 277-8583, Japan
[3] Department of Physics, Faculty of Science and Engineering, Konan University, Kobe, Hyogo 658-8501, Japan
[4] Institute of Astronomy, Graduate School of Science, The University of Tokyo, Mitaka, Tokyo 181-0015, Japan
[5] Institute for Theoretical and Experimental Physics (ITEP), Bolshaya Cheremushkinskaya 25, 117218 Moscow, Russia
[6] Novosibirsk State University, Novosibirsk 630090, Russia
[7] National Research Nuclear University MEPhI, 115409 Moscow, Russia
[8] All-Russia Research Institute of Automatics (VNIIA), 127055 Moscow, Russia
[9] Argelander Institute for Astronomy, University of Bonn, Auf dem Hügel 71, D-53121 Bonn, Germany
[10] Department of Physics, The University of Tokyo, Tokyo 113-0033, Japan
[11] Millennium Institute of Astrophysics, Casilla 36-D, Santiago, Chile
[12] Departamento de Astronomía, Universidad de Chile, Casilla 36-D, Santiago, Chile
[13] Research Center for Space and Cosmic Evolution, Ehime University, Matsuyama 790-8577, Japan
Received 2015 October 13; accepted 2016 January 8; published 2016 February 23

ABSTRACT

We present rapidly rising transients discovered by a high-cadence transient survey with the Subaru telescope and Hyper Suprime-Cam. We discovered five transients at $z = 0.384$–0.821, showing a rate of rise faster than 1 mag per day in the restframe near-ultraviolet wavelengths. The fast rate of rise and brightness are most similar to SN 2010aq and PS1-13arp, for which ultraviolet emission was detected within a few days after the shock breakout. The lower limit of the event rate of rapidly rising transients is ∼9% of core-collapse supernova rates, assuming the duration of rapid rise to be 1 day. We show that the light curves of the three faint objects agree with the cooling envelope emission from the explosion of red supergiants. The other two luminous objects, however, are brighter and faster than the cooling envelope emission. We interpret these two objects to be the shock breakout from a dense wind with a mass loss rate of $\sim 10^{-3}\ M_{\odot}\ \mathrm{yr}^{-1}$, as also proposed for PS1-13arp. This mass loss rate is higher than that typically observed for red supergiants. The event rate of these luminous objects is $\gtrsim$1% of the core-collapse supernova rate, and thus our study implies that more than ∼1% of massive stars can experience intense mass loss a few years before the explosion.

Key words: supernovae: general

1. INTRODUCTION

The transient sky has been explored intensively by various surveys in the last decade. In particular, optical surveys using wide-field cameras, such as the Palomar Transient Factory (Law et al. 2009; Rau et al. 2009), Catalina Real-Time Transient Survey (CRTS, Drake et al. 2009), and Pan-STARRS1 (PS1, e.g., Kaiser et al. 2010), have significantly contributed to building our knowledge of transient phenomena in the universe.

One of the important areas of discovery for transient surveys is phenomena with a short timescale, i.e., $\lesssim$1 day. There are, in fact, several theoretical expectations for such short-timescale transients. For supernovae (SNe), shock breakout emission should have a timescale of ∼1 hr for the case of red supergiant progenitors (e.g., Falk 1978; Klein & Chevalier 1978; Matzner & McKee 1999). The subsequent cooling emission lasts for a few days (e.g., Waxman et al. 2007; Chevalier & Fransson 2008; Nakar & Sari 2010). For the case of blue supergiants or Wolf–Rayet stars, these timescales are even shorter. Other possible short-timescale transients include, for example, the disk outflow from black-hole-forming SNe (< a few days, Kashiyama & Quataert 2015) and accretion-induced collapse of white dwarfs (∼1 day, Metzger et al. 2009). In addition to these, there might also be unknown kinds of transients with a short duration since our knowledge of short-timescale transients is still limited.

To explore the short-timescale transient sky, some dedicated high-cadence surveys have been started. For example, the Kiso Supernova Survey (KISS, Morokuma et al. 2014; Tanaka et al. 2014, using a 1.05 m Schmidt telescope and ∼4 deg^2 wide-field camera, Sako et al. 2012) and the High-cadence Transient Survey (HiTS, Forster et al. 2014, using the 4 m Blanco telescope and ∼3 deg^2 Dark Energy Camera, Flaugher et al. 2015) adopt ∼1 hr cadence, aiming at the detection of SN shock breakout. There are also some ambitious surveys to explore even shorter timescales (e.g., Becker et al. 2004; Rau et al. 2008; Berger et al. 2013), although no extragalactic transients with a timescale $\lesssim$30 minutes have been detected.

Recently, we have started a high-cadence transient survey with the 8.2 m Subaru telescope and 1.77 deg^2 Hyper Suprime-Cam (HSC, Miyazaki et al. 2006, 2012), as a part of the Subaru HSC Survey Optimized for Optical Transients (SHOOT). SHOOT also adopts ∼1 hr cadence, focusing on the detection of SN shock breakout (Tominaga et al. 2015a). In this paper, we present rapidly rising transients discovered in SHOOT. Here we define rapidly rising transients as objects that rise more than 1 mag in a day in the restframe, i.e., the rate of rise $|\Delta m/\Delta t| > 1\ \mathrm{mag\ day}^{-1}$. We describe our observations and

* Based (in part) on data collected at Subaru Telescope, which is operated by the National Astronomical Observatory of Japan.
[14] Hamamatsu Professor.

Table 1
Log of Observations

UT	Epoch	Instrument	Mode	Seeing[a] (arcsec)
2014 Jul 2	Day 1	HSC	imaging (g, r)	0.5
2014 Jul 3	Day 2	HSC	imaging (g, r)	0.6
2014 Aug 5	Day 35	FOCAS	imaging (g, r) spectroscopy	0.9
2014 Aug 6	Day 36	FOCAS	imaging (g, r) spectroscopy	0.9
2015 May 24	Day 327	HSC[b]	imaging (g, r)	1.0
2015 Jun 22	Day 356	FOCAS	spectroscopy	0.5
2015 Aug 19	Day 414	HSC[b]	imaging (r)	1.4

Notes.
[a] Full width at half-maximum.
[b] Used as reference images.

Table 2
Classification of Detected Sources

Classification: Number of Sources			
Total: 412			
Fake[a]: 215	Astronomical Objects: 197		
	Star/quasar[b]: 166	Non-star: 31	
		Center: 16 (8[c])	Offset: 15 (1[c])

Notes.
[a] Non-astronomical sources such as bad image subtraction, bad reference, or cosmic-ray events.
[b] Point sources (including moving objects with a negligible motion).
[c] Number of fading objects in the samples.

sample selection in Section 2. Then, we compare the obtained light curves with previously known SNe and transients in Section 3. Phase space of various transients is summarized in Section 4. Based on these comparisons, we discuss the nature of these transients in Section 5. Finally we draw conclusions in Section 6. Throughout the paper, we assume the following cosmological parameters: $\Omega_M = 0.273$, $\Omega_\Lambda = 0.726$, and $H_0 = 70.5\,\mathrm{km\,s^{-1}\,Mpc^{-1}}$ (Komatsu et al. 2009). All the magnitudes are given as AB magnitudes.

2. OBSERVATIONS AND SAMPLE SELECTION

2.1. HSC Observations

We performed a high-cadence transient survey with Subaru/HSC for two consecutive nights, 2014 July 2 and 3 UT (hereafter Day 1 and Day 2, respectively). The log of our observations is given in Table 1. Seven fields of view ($\simeq$12 deg^2) were visited repeatedly with about 1 hr cadence. Our survey was carried out mostly in the optical g-band, targeting the detection of the very early phase of SNe (Tominaga et al. 2015a). Within one night, we had three or four visits in the g-band (here one "visit" consists of five exposures of 2 minutes each). We also had one visit in the r-band on each night to obtain $g - r$ color.

The HSC data were reduced using the HSC pipeline (version 3.6.1) developed on the basis of the LSST pipeline (Ivezic et al. 2008; Axelrod et al. 2010). Five exposure images were co-added after standard reduction for each frame. We used the Sloan Digital Sky Survey DR8 catalog (Aihara et al. 2011) for astrometry and photometric calibration. For stacked images for one visit (i.e., 10 minutes exposure), a typical limiting magnitude is about 26 mag (3σ limiting magnitude for point sources) in both g- and r-bands.

We performed image subtraction using the HSC pipeline. The pipeline adopts the algorithm developed by Alard & Lupton (1998) and Alard (2000), which is used for the ISIS package[15] and the HOTPANTS package.[16] The algorithm uses a space-varying convolution kernel to match the point-spread functions (PSFs) of two images. The optimal convolution kernel is derived by minimizing the difference between convolved PSFs of two images. Although our seven survey fields are selected on the basis of the availability of the past imaging data, most of the survey fields lack imaging data that are deep and wide enough to be used as references for our new HSC images. Thus, we used the data taken on the first visit of Day 1 as reference images for sample selection.

The data reduction described above was performed in real time using the on-site data analysis system (Furusawa et al. 2011) and a dedicated transient system (Tominaga et al. 2015a). By using these systems, transient candidates were typically selected on the same night (Tominaga et al. 2014a, 2014b, 2015b, 2015c).

To obtain the final reference images, we also performed HSC imaging observations on 2015 May 24 UT (Day 327, for g- and r-bands) and 2015 August 19 UT (Day 414, for r-band). All the photometric values given in this paper are derived by aperture photometry with 7 pixel radius (1.18 arcsec) in the difference images using these final reference images.

2.2. Sample Selection

We adopted the following selection processes to select candidates for rapidly rising transients. As mentioned above, we used the first images taken on Day 1 as reference images for the selection process. Therefore, source detection in the subtracted images is sensitive only to objects showing variability over two nights.

Detected sources in the subtracted images contain not only real astronomical sources but also fake sources such as spikes around bright stars, and artifacts due to mis-subtraction or misalignment (e.g., Bailey et al. 2007; Bloom et al. 2012; Brink et al. 2013). Thus, we selected objects detected in the subtracted images at least twice with $>5\sigma$ significance. After this selection, 1407 sources remained. We first performed initial visual screening, resulting in 430 sources with SHOOT14XX names (412 independent sources because of 18 duplications in overlapped regions in the reduced images). Then, we further performed detailed classification. Results of the classifications are summarized in Table 2.

Among 412 independent sources, 215 sources are still fakes of the subtracted images while the other 197 sources are likely to be astronomical sources. The astronomical sources are dominated by stellar-shape sources, such as stars or quasars (166 sources). The remaining 31 sources are associated with extended sources (galaxies). Among these sources, 16 sources are located at the center of galaxies. Since they may be active galactic nuclei or tidal disruption events, we avoided these

[15] http://www2.iap.fr/users/alard/package.html
[16] http://www.astro.washington.edu/users/becker/v2.0/hotpants.html

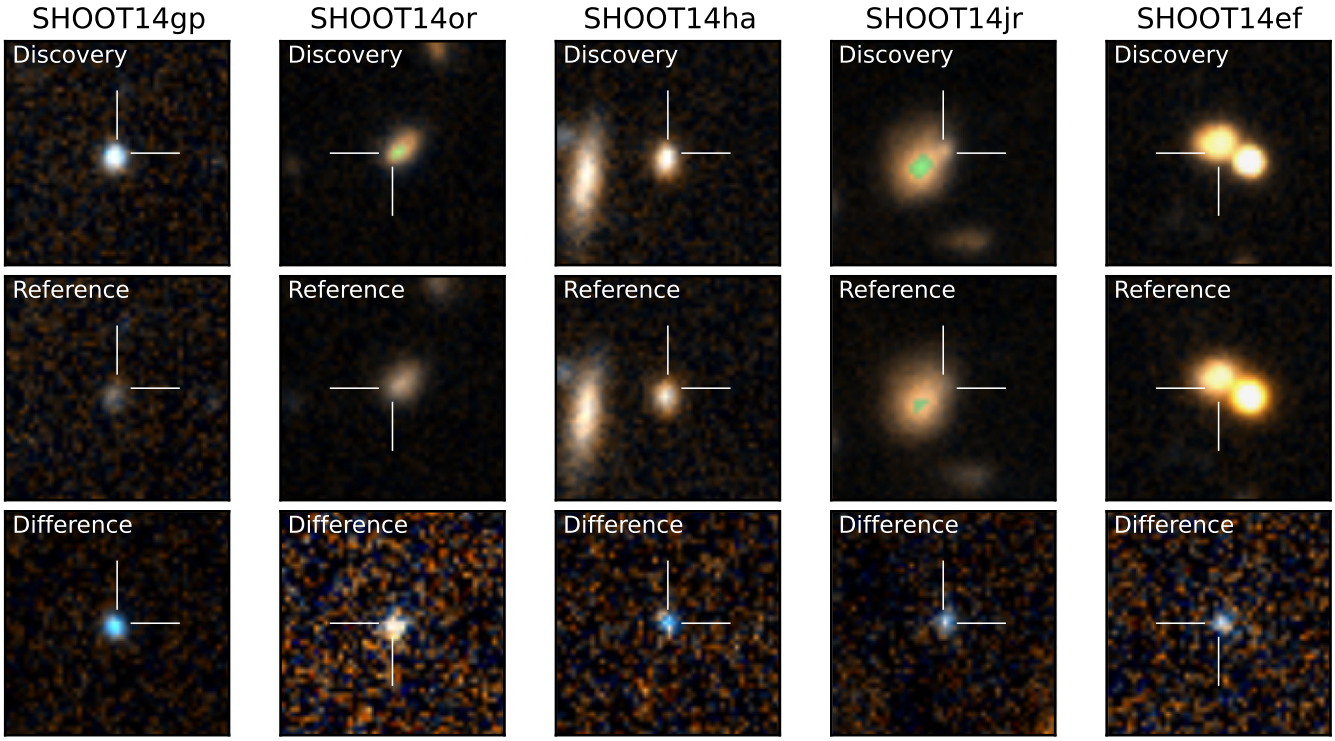

Figure 1. Images of rapidly rising transients (g- and r-band two-color composite images). From top to bottom, each panel shows the discovery images taken on Day 2, images taken on Day 1 (used as references for the sample selection), and difference images (Day 2 – Day 1). Each panel is of size $8'' \times 8''$. North is up and east is left. The color scales for the discovery and reference images are set to be the same.

objects for follow-up observations. Since 8 out of 16 objects show declining flux, it is likely that the majority of these 16 sources are active galactic nuclei. The remaining 15 sources have an offset from the center of the galaxies, and are selected as SN candidates.

The final SN candidates consist of 14 brightening objects. From this final sample, we performed follow-up observations of the 12 most reliable objects. Among these, we measured redshifts for eight of them while the other four (and their host galaxies) were too faint to take spectra. The remaining two objects were not observed.

Note that the sample selection for spectroscopy was made based on the *flux* difference over two nights, not on the *magnitude* difference since the final reference images were not available and true magnitudes of the objects on Day 1 were not known at the time of spectroscopy (2014 August). Therefore, even after the selection processes, our initial samples could include not only rapidly rising transients but also normal SNe around their peak brightness if the flux difference over two nights is large enough. In fact, our follow-up spectroscopic observations (Section 2.3) allowed us to identify three out of eight objects as normal SNe (at $z = 0.13$, 0.25, and 0.40). In addition, after obtaining the final reference images on Day 327, we confirmed that these three objects were already bright on Day 1. The rates of rise for these three objects are $|\Delta m/\Delta t| < 1$ mag day^{-1}, which is also consistent with normal SNe. Therefore, we omit these three objects from our samples.

Figure 1 shows images of five rapidly rising transients, named SHOOT14gp, 14or, 14 ha, 14jr, and 14ef (Table 3). Photometry of these five objects is shown in Table 4.

Table 3
Rapidly Rising Transients from the Subaru/HSC Transient Survey

Object	R.A. (J2000.0)	Decl. (J2000.0)	Redshift	$\lvert\Delta m/\Delta t\rvert$[a] (mag day^{-1})
SHOOT14gp	23:20:20.80	+28:25:00.54	0.635	>3.10
SHOOT14or	15:26:24.18	+47:47:07.34	0.821	$3.12^{+1.11}_{-0.70}$
SHOOT14ha	23:21:44.91	+28:54:49.80	0.548	>1.19
SHOOT14jr	16:33:49.99	+34:28:05.36	0.384	$1.61^{+0.39}_{-0.32}$
SHOOT14ef	21:31:08.77	+09:32:54.10	0.560	>1.31

Note.
[a] Measured in g-band data. Errors represent 1σ. For the objects that are not detected in the difference images on Day 1 (Day 1 – Day 327), 3σ lower limits are given.

2.3. Follow-up Observations

We performed imaging and spectroscopic observations of five objects (Table 3) using the Faint Object Camera and Spectrograph (FOCAS, Kashikawa et al. 2002) of the Subaru telescope. Observations of four objects (SHOOT14gp, 14or, 14 ha, and 14jr) were carried out on 2014 August 5 and 6 UT (Days 35 and 36, respectively) while observations of SHOOT14ef were made on 2015 June 22 (Day 356, only for the host galaxy).

For the FOCAS imaging data, we performed image subtraction with the final reference images using the HOTPANTS package. SHOOT14gp and 14or were only marginally detected in the r-band while they were not detected in the g-band. The other objects were not detected in either g- or r-band. Typical limiting magnitudes are $\simeq$25.0–25.5 mag (Table 4).

Table 4
Photometry of Rapidly Rising Transients

MJD	Filter	Magnitude[a]	Instrument
		SHOOT14gp	
56840.542	g	>25.53	HSC
56840.577	g	>25.57	HSC
56841.513	g	$23.74^{+0.09}_{-0.08}$	HSC
56841.547	g	$23.72^{+0.08}_{-0.07}$	HSC
56841.582	g	$23.70^{+0.08}_{-0.07}$	HSC
56840.560	g	>25.58	HSC[b]
56841.548	g	$23.71^{+0.07}_{-0.06}$	HSC[b]
56874.475	g	>25.45	FOCAS
56840.479	r	>24.99	HSC
56841.456	r	$24.31^{+0.15}_{-0.13}$	HSC
56874.463	r	$25.51^{+0.63}_{-0.39}$	FOCAS
		SHOOT14or	
56840.287	g	$26.74^{+0.65}_{-0.40}$	HSC
56840.332	g	$26.88^{+0.75}_{-0.44}$	HSC
56841.283	g	$25.11^{+0.13}_{-0.12}$	HSC
56841.326	g	$25.01^{+0.12}_{-0.10}$	HSC
56841.487	g	$24.99^{+0.11}_{-0.10}$	HSC
56840.310	g	$26.85^{+0.64}_{-0.40}$	HSC[b]
56841.365	g	$25.04^{+0.08}_{-0.07}$	HSC[b]
56873.315	g	>25.69	FOCAS
56840.431	r	>25.61	HSC
56841.412	r	$25.25^{+0.25}_{-0.20}$	HSC
56873.276	r	$25.79^{+0.59}_{-0.38}$	FOCAS
		SHOOT14ha	
56840.542	g	>25.77	HSC
56840.577	g	>25.79	HSC
56841.513	g	$25.29^{+0.33}_{-0.25}$	HSC
56841.547	g	$25.27^{+0.28}_{-0.22}$	HSC
56841.582	g	$24.95^{+0.19}_{-0.16}$	HSC
56840.560	g	>25.87	HSC[b]
56841.548	g	$25.11^{+0.20}_{-0.17}$	HSC[b]
56874.601	g	>25.42	FOCAS
56840.479	r	>25.48	HSC
56840.479	r	>25.48	HSC
56841.456	r	$25.26^{+0.32}_{-0.25}$	HSC
56873.501	r	>25.03	FOCAS
56874.589	r	>25.07	FOCAS
		SHOOT14jr	
56840.299	g	$25.85^{+0.33}_{-0.25}$	HSC
56840.342	g	$25.96^{+0.37}_{-0.27}$	HSC
56840.526	g	$25.50^{+0.26}_{-0.21}$	HSC
56841.293	g	$24.65^{+0.10}_{-0.09}$	HSC
56841.338	g	$24.77^{+0.12}_{-0.11}$	HSC
56841.500	g	$24.45^{+0.08}_{-0.08}$	HSC
56840.389	g	$25.76^{+0.27}_{-0.21}$	HSC[b]
56841.377	g	$24.61^{+0.09}_{-0.08}$	HSC[b]
56840.442	r	$25.84^{+0.72}_{-0.43}$	HSC
56841.422	r	$24.87^{+0.23}_{-0.19}$	HSC
56873.262	r	>25.36	FOCAS
		SHOOT14ef	
56840.554	g	>26.30	HSC
56840.591	g	>26.41	HSC
56840.610	g	>26.19	HSC
56841.525	g	$25.57^{+0.22}_{-0.18}$	HSC
56841.559	g	$25.72^{+0.23}_{-0.19}$	HSC
56841.596	g	$25.70^{+0.27}_{-0.21}$	HSC
56841.615	g	$25.74^{+0.30}_{-0.23}$	HSC
56840.585	g	>26.50	HSC[b]
56841.574	g	$25.67^{+0.20}_{-0.17}$	HSC[b]
56840.467	r	>26.08	HSC
56841.445	r	>26.06	HSC

Notes.
[a] All the photometry is derived from the subtracted images using the final reference images. Errors represent 1σ. For the cases of non-detection, 3σ upper limits are given. Magnitudes are corrected only for Galactic extinction.
[b] Photometry in the one-night stack images.

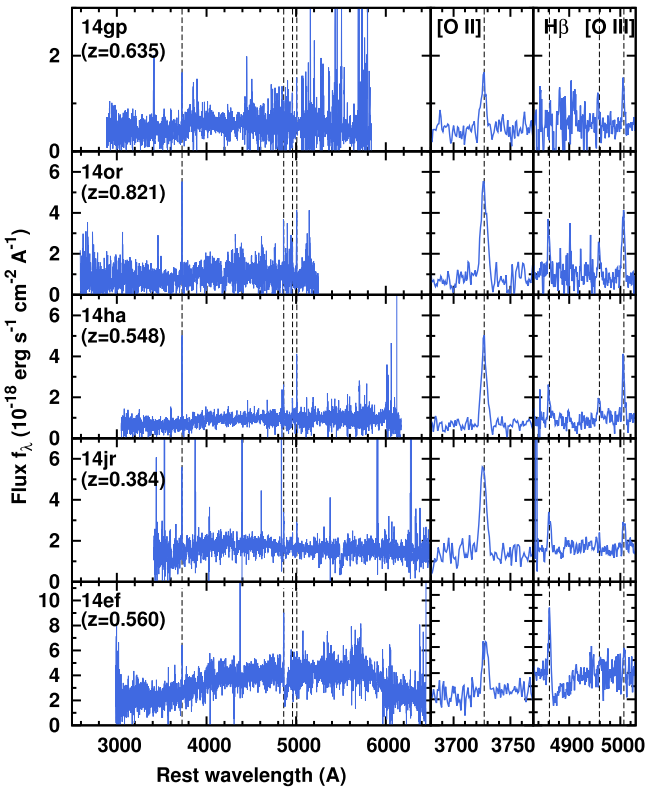

Figure 2. Spectra of host galaxies of SHOOT14gp, 14or, 14 ha, 14jr, and 14ef (from top to bottom). The wavelengths of strong emission lines ([O II] λ3727, Hβ, and [O III] $\lambda\lambda$4959, 5007) are marked with dashed lines. The right panels show the data around these lines.

For spectroscopy, we used the multi-object mode with a 0.″8 wide slit and the long-slit mode with a 1.″0 wide slit (only for SHOOT14ef). With the 300B (300 lines mm^{-1}) grism and the SY47 order-sort filter, our configuration gives a wavelength coverage of 4700–9000 Å and a spectral resolution of $R = \lambda/\Delta\lambda \sim 600$. The data were reduced with the IRAF packages in a standard manner.

The transient components are not detected in our spectra, as expected from the results of imaging observations. Figure 2 shows the spectra of the host galaxies for these five objects.

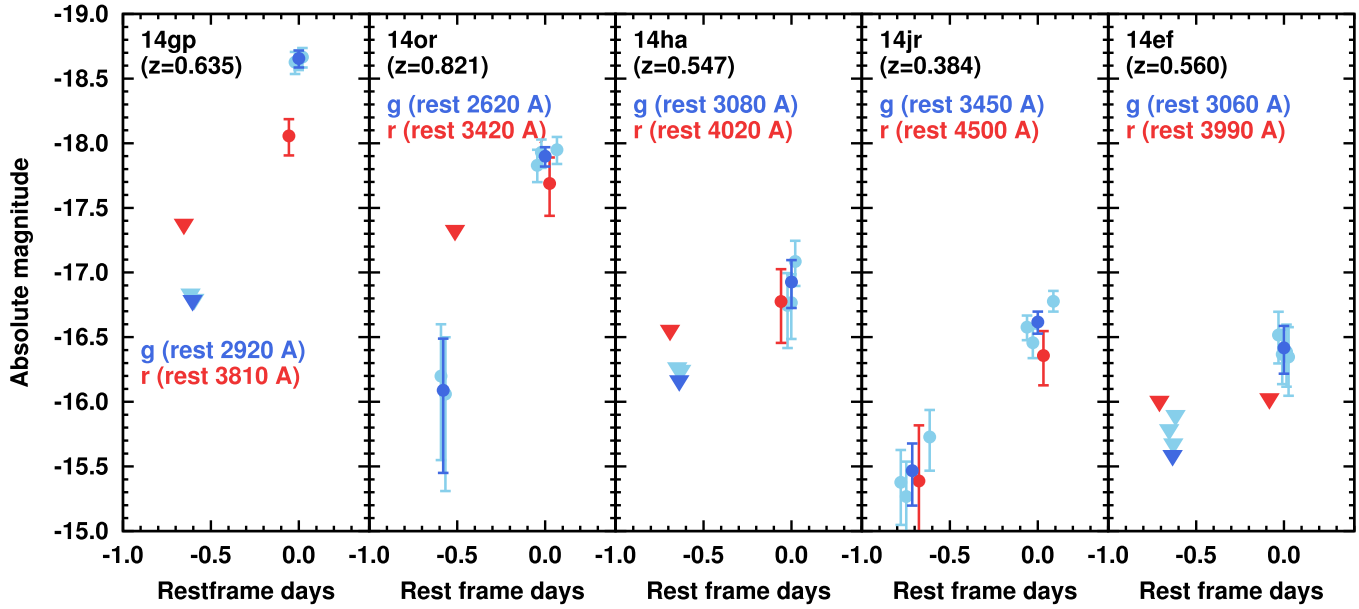

Figure 3. Light curves of the five rapidly rising transients on Days 1 and 2. The g- and r-band photometry is shown by the blue and red points, respectively. Triangles show the 3σ upper limit. For the g-band data, photometry for one visit (5×2 minute exposures) is shown in pale blue while photometry in the one-night stacked data is shown in blue.

The [O II] λ3727 emission line is detected from all the host galaxies, which indicates that they are all star-forming galaxies. The redshifts range from $z = 0.384$ (SHOOT14jr) to $z = 0.821$ (SHOOT14or).

3. LIGHT CURVES

3.1. Overview

Figure 3 shows light curves of our samples on Day 1 and Day 2. Hereafter, the epochs of stacked g-band data on Day 2 are taken to be $t = 0$ unless otherwise mentioned. The photometry is performed in the subtracted images using the final references (e.g., Day 1 – Day 327 and Day 2 – Day 327 for the g-band).

Throughout the paper, we do not take into account full K-correction for absolute magnitudes since only limited information about the spectral energy distribution is available for our samples. Instead, we correct only the effect of redshifts, i.e., $M = m - \mu + 2.5\log(1 + z)$, where M and m are absolute and observed AB magnitudes (measured as f_ν) and μ is the distance modulus. The last term originates from the difference in the frequency bins in the restframe and observer frame, i.e., $L_\nu(\nu_e) = [(4\pi d^2)/(1 + z)]f_\nu(\nu_o)$, where ν_e and ν_o are restframe and observer frame frequencies, and d is the luminosity distance (Hogg et al. 2002).

The absolute magnitudes of the five objects range from -16 to -19 mag in the restframe near-ultraviolet (UV) wavelengths (2620–3450 Å, depending on the redshifts). The photometric values of our samples are corrected for extinction in our Galaxy but not for extinction in the host galaxy. Therefore, intrinsic absolute magnitudes can be brighter than those shown in Figure 3.

All of the five objects show a blue $g - r$ color on Day 2, $g - r \simeq -0.60$, -0.21, -0.15, and -0.15 mag for SHOOT14gp, 14or, 14 ha, and 14jr, respectively. For SHOOT14ef, the color is $g - r < -0.39$ mag. This indicates that, for the blackbody case, the peak of the spectra is located at wavelengths shorter than the wavelengths corresponding to the observed r-band. Therefore the blackbody temperatures for our objects are $T_{\rm BB} \gtrsim 13{,}000$, 15,000, 13,000, 11,000, and 13,000 K for SHOOT14gp, 14or, 14 ha, 14jr, and 14ef, respectively. Note that the intrinsic colors can be bluer due to the extinction in the host galaxies.

SHOOT14or and 14jr are detected in the images of Day 1 – Day 327. We measure the rates of rise from Day 1 to Day 2 using the g-band one-day stacked images: $|\Delta m/\Delta t| = 3.12^{+1.11}_{-0.70}$ and $1.61^{+0.39}_{-0.32}$ mag day^{-1} for SHOOT14or and 14jr, respectively (errors represent 1σ, Table 3). Note that the rate of rise is measured in the restframe, so the time interval used for the measurement varies with the source redshift ($\Delta t = 0.55$ days for SHOOT14or while $\Delta t = 0.72$ days for SHOOT14jr). The other three objects (SHOOT14gp, 14 ha, and 14ef) are not detected in the subtracted images of Day 1 – Day 327. The 3σ lower limits of the rate of rise measured in the g-band are $|\Delta m/\Delta t| > 3.10$, 1.21, and 1.17 mag day^{-1}. These are also high enough to match our criterion for rapidly rising transients.

In the following sections, we compare the light curves of our samples with those of previously known SNe and transients.

3.2. Comparison with SNe

Figure 4 shows a comparison of rapidly rising transients with normal SNe. Since the redshifts of our samples are moderately high, $z = 0.384$–0.821, we compare our g- and r-band light curves with near-UV and u-band light curves of nearby SNe with good temporal coverage. We use the *Swift* $uvw1$- and u-band data from Brown et al. (2012) and Pritchard et al. (2014) with extinction correction (both in our Galaxy and host galaxies) using the extinction law of Brown et al. (2010). Since the effective restframe wavelengths do not always match perfectly, we always give effective restframe wavelengths in parenthesis.

Figure 4 shows that the properties of our samples are not consistent with those of SNe Ia at any phase, or those of core-collapse SNe more than a few days after the explosion. The

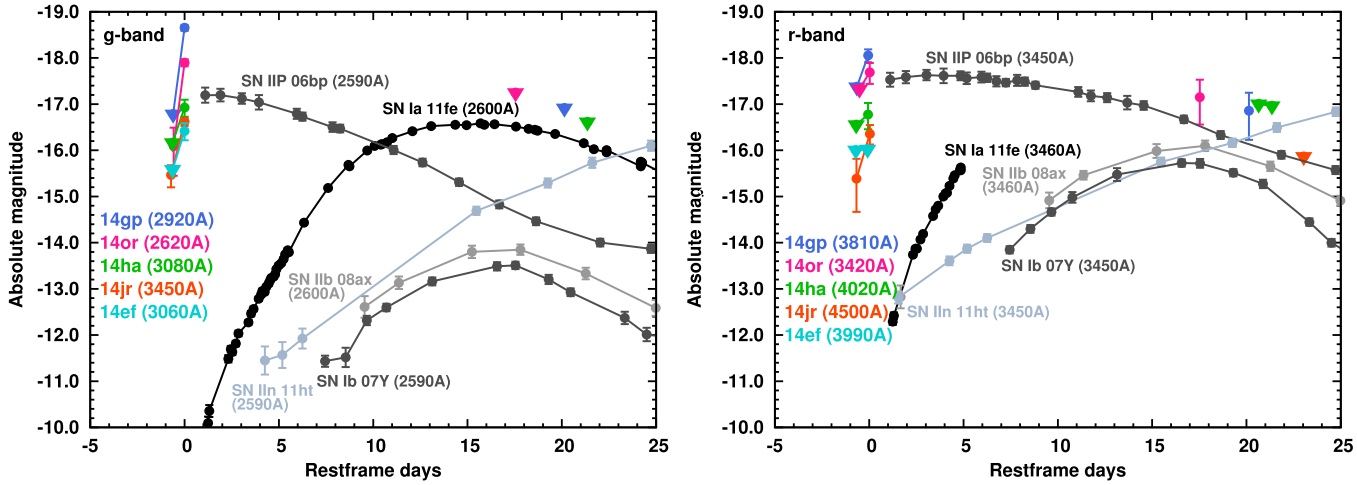

Figure 4. Left: comparison between g-band light curves of our objects and *Swift* $uvw1$-band light curves of nearby normal SNe: SN Ia 2011fe (Brown et al. 2012), SN IIP 2006bp, SN IIb 2011dh, SN IIn 2011ht, and SN Ib 2007Y (Pritchard et al. 2014). Right: comparison between r-band light curves of our objects and *Swift* u-band light curves. For *Swift* SN data, the estimated epoch of the explosion is taken to be $t = 0$ day. The *Swift* data are corrected for the extinction in both our Galaxy and host galaxies as estimated by Pritchard et al. (2014). Vega magnitudes are converted to AB magnitudes using the zero-points presented by Breeveld et al. (2011).

absolute magnitudes of our samples are as luminous as the peak magnitudes of SN Ia 2011fe (Brown et al. 2012) and SN IIP 2006bp (Pritchard et al. 2014). However, the rates of rise for our samples are faster than the very early phase of SN 2011fe, one of the best observed SNe Ia. We also compare our objects with SN IIb 2008ax, SN IIn 2011ht, and SN Ib 2007Y (Pritchard et al. 2014). Their rates of rise are slower than those of our samples at any epoch with available data, i.e., more than a few days after the explosion. In addition, the blue colors of our samples ($g - r \leqslant -0.2$ mag) are not consistent with normal SNe more than a few days after the explosion. For nearby SNe, the $uvw1$ magnitude is generally fainter than the u magnitude as shown in Figure 4, i.e., the color is $uvw1 - u > 0$ mag.

Our samples might correspond to the rising phase of much brighter SNe, such as superluminous SNe (SLSNe, Quimby et al. 2011; Gal-Yam 2012). Figure 5 shows a comparison of our samples with SLSNe SN 2010gx, PS1-10awh, and PS1-10ky with a good temporal coverage (Pastorello et al. 2010; Chomiuk et al. 2011). Our data on Days 1 and 2 could be interpreted as the very early phase of SLSNe, which have never been caught. However, the data on Days 35 and 36 are clearly inconsistent with the declining part of SLSNe. Note that Arcavi et al. (2015) recently reported transients with luminosities between those of SNe and SLSNe, and our samples can be consistent with such a class of objects.

3.3. Comparison with the Very Early Phase of SNe

We compare our samples with earlier phases of SNe (less than a few days after the explosion). First, we show comparison with SN IIP 2010aq (Gezari et al. 2010) and PS1-13arp (Gezari et al. 2015), with UV detection at the very early phase with *GALEX*. The early emission of SN 2010aq is consistent with cooling envelope emission after SN shock breakout (Gezari et al. 2010). Note that larger samples with *GALEX* UV detection are presented by Ganot et al. (2014) and the emission is also consistent with the cooling envelope emission. The emission of PS1-13arp is brighter and shorter, which may indicate shock breakout emission from a dense wind (Gezari et al. 2015).

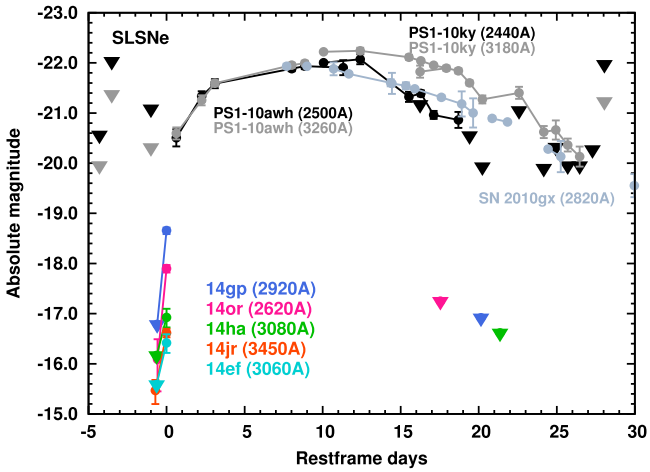

Figure 5. Comparison of light curves with SLSNe (Pastorello et al. 2010; Chomiuk et al. 2011). Observed u-band light curves are shown for SN 2010gx, while observed g- and r-band light curves are shown for PS1-10awh and PS1-10ky. For SLSNe, the peak epochs are shifted to $t = 13$ days and magnitudes are corrected for only Galactic extinction.

The left-hand panel of Figure 6 shows a similarity of the rate of rise and the brightness between our samples and SN 2010aq and PS1-13arp. SN 2010aq and PS1-13arp also show fast rises, $|\Delta m/\Delta t| > 0.989$ and >2.635 mag day^{-1}, respectively. They reach about -17 to -18 mag, which is also similar to our samples. Note that the effective restframe wavelengths corresponding to the NUV filter of *GALEX* (2130 Å for SN 2010aq and 1990 Å for PS1-13arp) are shorter than those for our samples (~2600–3500 Å).

For comparison, we also show the non-filter magnitude of SN IIP 2006bp (Quimby et al. 2007), for which very early phases were observed (see also González-Gaitán et al. 2015, Gall et al. 2015, and Rubin et al. 2015 for recent larger samples). It also shows a fast rise, $|\Delta m/\Delta t| = 2.3$ mag day^{-1}. Similarly, Type IIb SN 2013cu, whose emission was caught at extremely early phases by Gal-Yam et al. (2014), shows $|\Delta m/\Delta t| \sim 2$ mag day^{-1} in the r-band. Again, although the

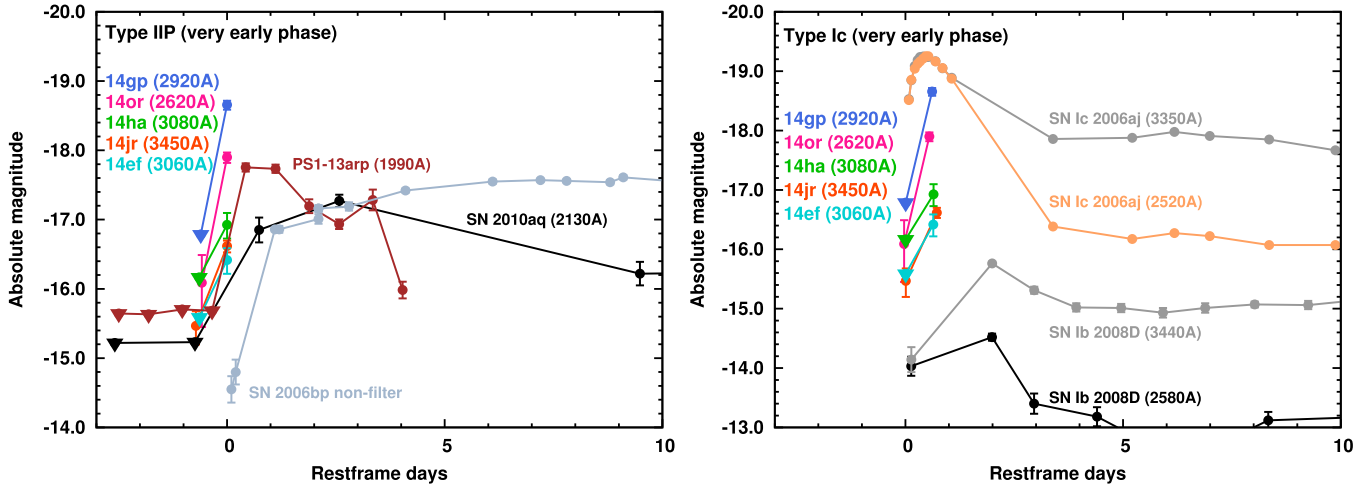

Figure 6. Left: comparison of light curves with the very early phase of SNe IIP: *GALEX* NUV data of SN IIP 2010aq (Gezari et al. 2010) and PS1-13arp (Gezari et al. 2015), and also non-filter data of SN 2006bp (Quimby et al. 2007). The data of SN 2010aq and PS1-13arp are corrected for only Galactic extinction while those of SN 2006bp are corrected for both Galactic and host extinction. Right: comparison with the very early phase of SN Ic 2006aj (Campana et al. 2006; Šimon et al. 2010, corrected for only Galactic extinction) and SN Ib 2008D (Modjaz et al. 2009, corrected for both Galactic and host extinction). For the comparison with SNe Ibc, the epoch of our data is shifted so that Day 1 corresponds to $t = 0$ day.

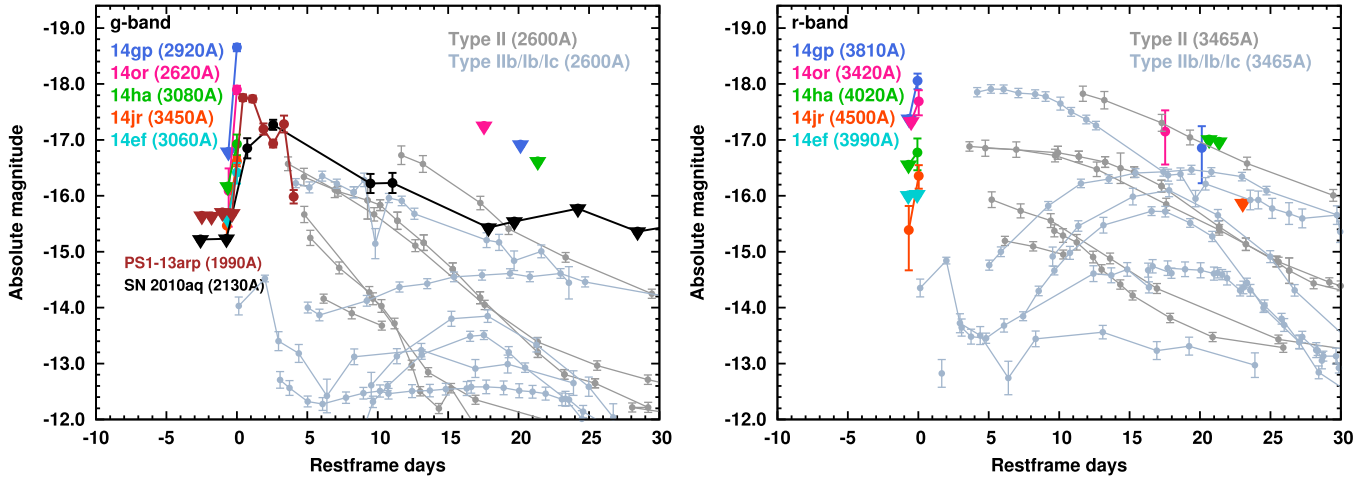

Figure 7. Left: comparison between *g*-band light curves of our objects and *Swift uvw*1-band light curves of core-collapse SNe (Modjaz et al. 2009; Pritchard et al. 2014) and SN IIP 2010aq (Gezari et al. 2010) and PS1-13arp (Gezari et al. 2015) with *GALEX* NUV data. Right: comparison between *r*-band light curves of our objects and *Swift u*-band light curves of core-collapse SNe. The data from Pritchard et al. (2014) are corrected for estimated extinction in both our Galaxy and host galaxies. Vega magnitudes are converted to AB magnitudes.

difference in the restframe wavelengths should be mentioned, these similarities suggest that our samples of rapidly rising transients are the very early phase of SNe.

We also compare our samples with the very early part of SN Ic 2006aj and SN Ib 2008D. They are among the best-studied stripped-envelope SNe. SN 2006aj is associated with low-luminosity gamma-ray burst 060218, and thus good optical to NUV data are available from soon after the explosion (e.g., Campana et al. 2006; Mazzali et al. 2006; Mirabal et al. 2006; Modjaz et al. 2006; Pian et al. 2006; Soderberg et al. 2006; Sollerman et al. 2006; Šimon et al. 2010). SN 2008D is associated with X-ray transient 080109 (e.g., Mazzali et al. 2008; Soderberg et al. 2008; Modjaz et al. 2009; Tanaka et al. 2009a, 2009b). Emission from the first two days of SN 2006aj and SN 2008D is interpreted as cooling envelope emission (Waxman et al. 2007; Chevalier & Fransson 2008; Soderberg et al. 2008; Modjaz et al. 2009; Nakar 2015).

The right-hand panel of Figure 6 shows that the rate of rise of SN 2006aj is as fast as our samples. The time to the peak is only ∼0.5 days, which is as short as that inferred for our samples although we cannot not firmly determine the peak dates with data from only two nights. SN 2008D lacks the data at ∼1 day after the explosion. Nevertheless, the rate of rise of SN 2008D in *Swift u*-band (measured with a 2 day interval) is similar to that of SHOOT14jr. Note that if the early part of SN 2008D is interpreted as cooling envelope emission, the peak would be around one day after the explosion (Soderberg et al. 2008; Modjaz et al. 2009), and the rate of rise on the first day is faster than that measured with a 2 day interval.

When we match our objects with core-collapse SNe within a few days after the explosion, our observations on Days 35 and 36 correspond to the plateau phase of Type IIP or the peak phase of SNe Ibc. As shown in Figure 7, the distribution of *uvw*1 brightness of core-collapse SNe at these epochs ranges from −12 to −17 mag. Since our limits in the *g*-band correspond to −17.0 mag, non-detection in the *g*-band on Days 35 and 36 is not surprising. SHOOT14gp and 14or are marginally detected in the *r*-band (right panel of Figure 7).

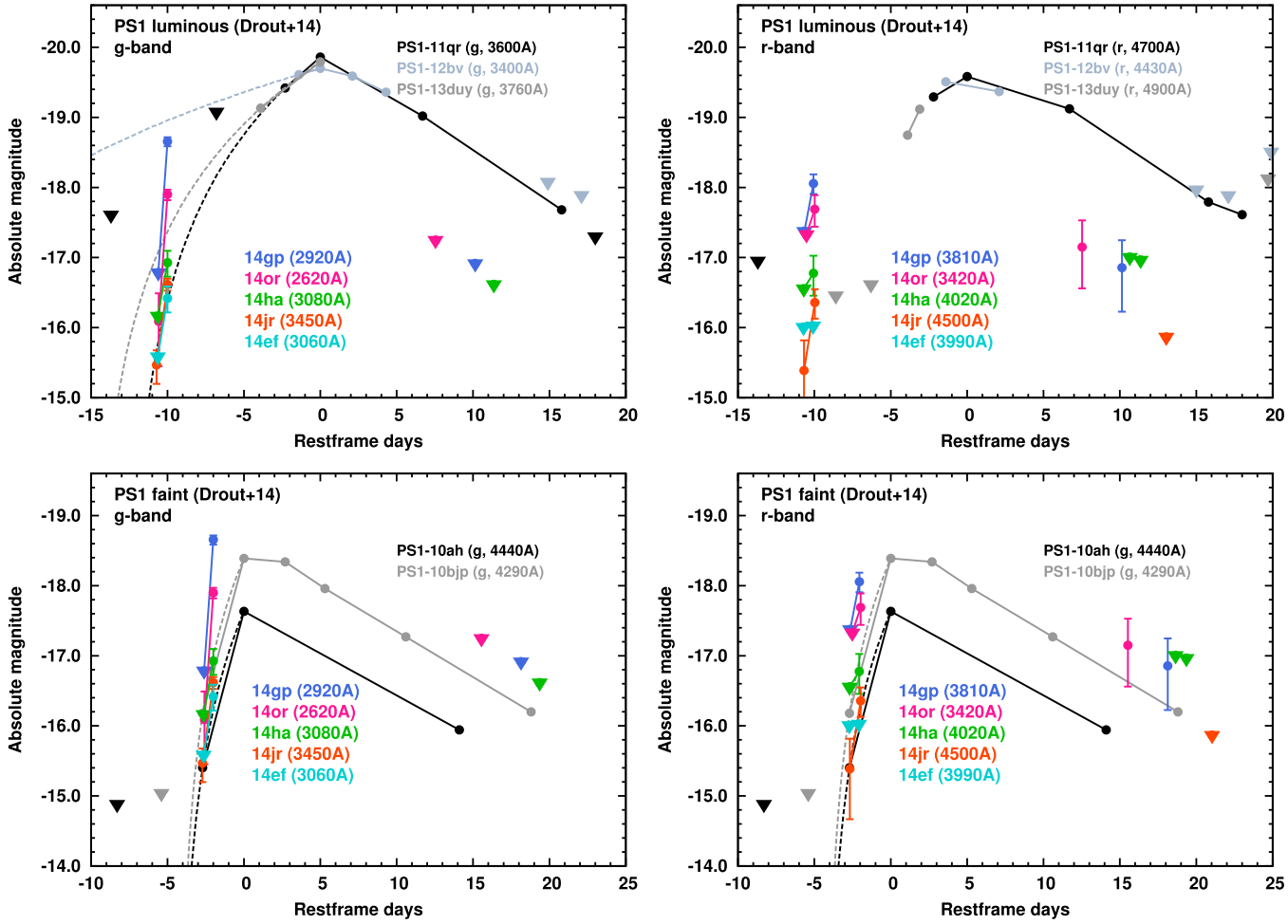

Figure 8. Comparison of light curves with rapidly evolving and luminous transients from PS1 (Drout et al. 2014). The peak epoch of the PS1 samples is selected to be $t = 0$ day. Upper: comparison with the PS1 luminous samples with peak absolute magnitudes of <-19 mag. Left and right panels show the light curves in g- and r-bands (both for HSC and PS1), respectively. Epochs of our samples are shifted so that Day 2 data correspond to $t = -10$ days. Lower: comparison with the PS1 faint samples with peak absolute magnitudes of >-19 mag. Left and right panels show the light curves in g- and r-bands for HSC data, respectively. For the PS1 sample, g-band data are shown in both panels (as the g-band has closer effective wavelengths). Epochs of our samples are shifted so that Day 2 data correspond to $t = -2$ days. The magnitudes of the PS1 samples are corrected for only Galactic extinction.

Compared with *Swift* u-band data, their brightness is consistent with those of core-collapse SNe at the luminous end.

3.4. Comparison with Rapidly Rising Transients from PS1

The rapid rates of rise of our samples remind us of a population of rapidly evolving and luminous transients from PS1, which are compiled by Drout et al. (2014, see also Kasliwal et al. 2010; Poznanski et al. 2010; Drout et al. 2013). These transients show rapid luminosity evolution in both rising and declining phases compared with normal SNe, with a time above half-maximum of less than 12 days. Interestingly, they show a faster rate of rise than rate of decline, which motivates the comparison with our samples. In addition, they have blue $g - r$ colors ($g - r < -0.2$ mag), similar to our samples.

Since the PS1 samples have a wide luminosity range, we divide the samples into two classes with absolute magnitude brighter (hereafter PS1 luminous samples) or fainter (PS1 faint samples) than -19.0 mag. Drout et al. (2014) interpret their rapid transients to be either (1) the cooling envelope emission following shock breakout (especially for faint samples) or (2) shock breakout from a dense wind (for luminous samples).

Figure 8 shows a comparison of our samples with the PS1 samples (Drout et al. 2014) where the rising part is detected in the g-band. The peak dates of the PS1 samples are taken to be $t = 0$ day. It should be cautioned that the PS1 samples have a wider redshift range than ours, and thus the rest wavelengths corresponding to the observed filters have a wider variety. For the PS1 luminous samples, g- and r-band data for our samples are compared with PS1 g- and r-band data, respectively. Since the PS1 faint samples have low redshifts ($z = 0.074$ for PS1-10ah and $z = 0.113$ for PS1-10bjp), we compare our g- and r-band data with PS1 g-band data.

The peak magnitudes of the PS1 luminous samples are brighter than the magnitudes of our samples on Day 2. Our samples could thus be interpreted as the rising part of the PS1 samples. The dashed lines in the upper left panel of Figure 8 shows the extrapolation of the rising part by assuming that the flux rises as $f \propto (t - t_0)^2$ (as often assumed for the early part of SNe, see, e.g., Nugent et al. 2011; Pastorello et al. 2013; Prieto et al. 2013; Yamanaka et al. 2014), where t_0 is the epoch with zero flux. Three of our samples (SHOOT14ha, 14jr, and 14ef) show a nice agreement with the extrapolated rising part if the epochs of these objects are shifted so that Day 2

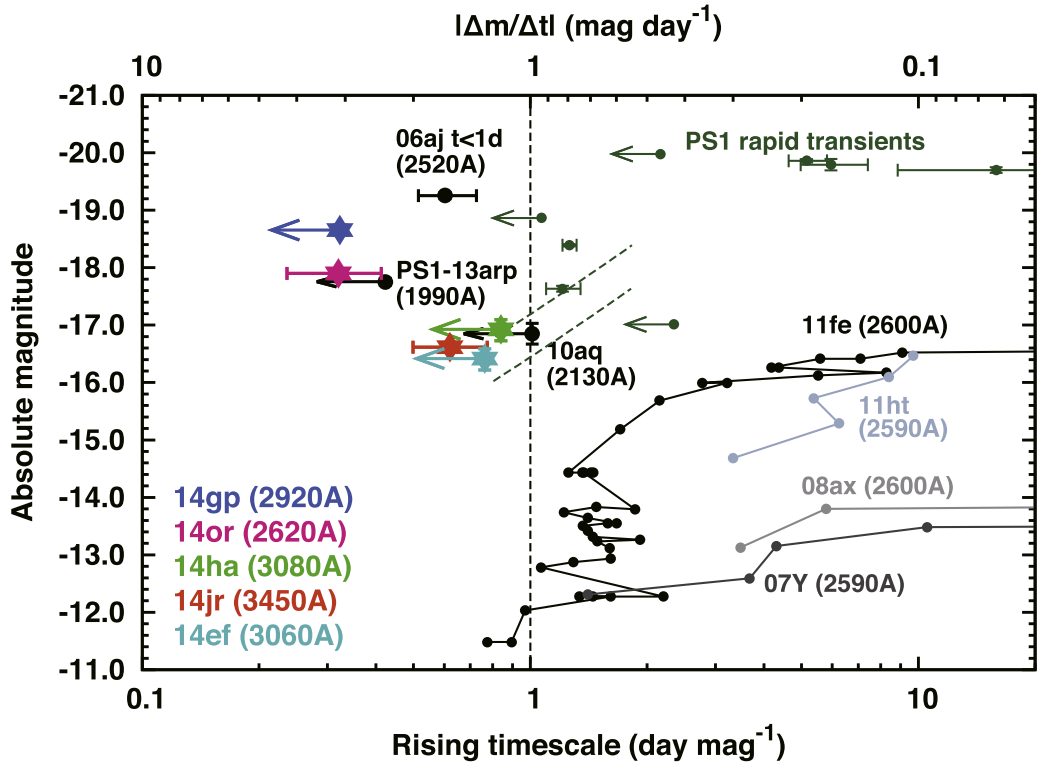

Figure 9. Summary of absolute magnitudes and rising timescale ($\tau_{\rm rise} \equiv 1/|\Delta m/\Delta t|$) of transients. Our samples are compared with the following objects: SN 2010aq and PS1-13arp (Gezari et al. 2010, 2015) with early UV detection with *GALEX*, the early peak of SN 2006aj (Campana et al. 2006; Šimon et al. 2010, Figure 6), SN Ia 2011fe (Brown et al. 2012), core-collapse SNe (SN Ib 2007Y, SN IIb 2008ax, and SN IIn 2011ht, Pritchard et al. 2014), and rapid transients from PS1 (Drout et al. 2014). For rapid transients from PS1, the rising timescale (rate of rise) is measured with *g*-band data. The dashed lines show the absolute magnitude and rising timescale of PS1-10ah and PS1-10bjp measured with the interpolated *g*-band light curves.

corresponds to $t \sim -10$ days. However, with this assumption, the non-detection of PS1-13duy before the peak in the *r*-band is not consistent with our detection on Day 2. In addition, the brightness and upper limits at later epochs (Days 35 and 36) are much fainter than the magnitudes of PS1-11qr, for which the data in the declining part are available. Therefore, our samples are not likely to be the same population as the PS1 luminous samples.

Our samples show a better agreement with the PS1 faint samples (lower panels of Figure 8). The rate of rise of the PS1 samples in the *g*-band is $|\Delta m/\Delta t| < 1$ mag day^{-1}, which does not fulfil our criterion. However, PS1 data are taken with ~3 days cadence, and thus the rate of rise measured with a shorter interval can be faster. In fact, if the rising part is interpolated with $f \propto (t - t_0)^2$, the rate of rise can be as fast as that measured for our samples. In particular, three of our samples (SHOOT14ha, 14jr, and 14ef) show a good match if the epochs of these objects are shifted so that Day 2 corresponds to $t \sim -2$ days. Then, our data at later epochs are also consistent with the PS1 samples in the declining phase. Since the estimated epoch of zero flux for PS1-10ah and PS1-10bjp is $t_0 \sim -4.2$ days from the peak, the epochs of our observations correspond to ~1.5–2.2 days after the explosion.

The agreement between the two luminous objects in our samples (SHOOT14gp and 14or) and PS1 faint samples is not as good as that for the three faint objects (SHOOT14ha, 14jr, and 14ef). Note that a direct comparison at perfectly matched wavelengths is not possible (<3000 Å for SHOOT14gp and 14or but >4000 Å for the PS1 faint samples). Nevertheless, SHOOT14gp and 14or show faster rises than the PS1 faint samples. The rates of rise of SHOOT14gp and 14or are >3.10 and $3.12^{+1.11}_{-0.70}$ mag day^{-1}, respectively (Table 3). On the other hand, the rate of rise of the PS1 faint sample is $|\Delta m/\Delta t| < 1.3$ mag day^{-1} even at the fastest phase in the interpolated light curves (see dashed lines in Figures 8 and 9). The nature of these objects is discussed in Section 5.

4. PHASE SPACE OF TRANSIENTS

Figure 9 shows a summary of the rate of rise and absolute magnitudes of our samples and other transients shown in Figures 4, 6, and 8. The figure is shown as a function of rising timescale $\tau_{\rm rise} \equiv 1/|\Delta m/\Delta t|$, the time for a rise of 1 mag. See, e.g., Rau et al. (2009), LSST Science and Collaboration (2009), Kasliwal (2012) and Arcavi (2015) for similar phase-space diagrams. For our objects, SN 2010aq, PS1-13arp, and the PS1 samples, the rates of rise are measured only at an interval on the rise as there are no time-series data before the peak. The time interval is $\Delta t \gtrsim 0.5$ days. For normal SNe, for which good time-series data are available, we measure the rate of rise $|\Delta m/\Delta t|$ as a function of time (connected with lines in Figure 9). In order to match the time interval with other objects, it is kept at $\Delta t \gtrsim 0.5$ days. For example, although fine time-series data are available for SN 2006aj before the peak, we measure the rate of rise from $t = 0.082$ and $t = 0.541$ days from the burst ($\Delta t_{\rm rest} = 0.45$ days). For the PS1 faint samples (PS1-10ah and PS1-10bjp), the green dashed lines show the rate of rise measured with $\Delta t_{\rm rest} = 0.5$ days using the light curves interpolated with $f \propto (t - t_0)^2$.

In this diagram, as also discussed in Section 3.2, it is clear that SNe Ia show the fast rise only in the very early phase with

faint magnitudes. Core-collapse SNe a few days after the explosion are located in a region with fainter magnitudes and longer timescales than our samples.

Our samples share a region similar to SN 2010aq and PS1-13arp, SNe with early UV detection by *GALEX* (Gezari et al. 2010, 2015), as expected from the comparison in the previous sections (Figure 6). The early peak of SN 2006aj also has a similar rate of rise, but it is brighter than our samples.

The PS1 luminous samples (Drout et al. 2014) are located in the region with brighter magnitudes and longer timescales. On the other hand, the PS1 faint samples are closer to the three faint objects in our samples (SHOOT14ha, 14jr, and 14ef). In particular, when the rate of rise is measured with the interpolated light curves to have a similar $\Delta t_{\rm rest}$ to our samples, the brightness and the rising timescale of the PS1 faint samples show fairly good agreement with SHOOT14ha, 14jr, and 14ef (see also Figure 8).

5. DISCUSSION

The properties of our samples of rapidly rising transients are similar to those of very early core-collapse SNe, such as SN 2010aq, PS1-13arp, and SN 2006aj (Figure 9). The three faint objects also show a similarity to the faint population (with > -19 mag) of the rapidly rising transients from PS1 (Drout et al. 2014), which are also interpreted as the very early phase of SNe. For both cases, the best match is obtained when our samples are assumed to be ~1–2 days after the explosion.

From these facts, although we do not have photometric follow-up and spectroscopic identification of our samples, we interpret that the rapidly rising transients presented in this paper are the very early phase of core-collapse SNe. In the following sections, we discuss the nature of the rapidly rising transients based on this interpretation.

5.1. Constraints on the Event Rate

Event rates of rapidly rising transients shown in this paper are of interest. However, to estimate the event rates, we need detailed information about spectral energy distribution, light curve shape, and luminosity function, which are not available for our samples. Instead, we give crude constraints on how high an event rate is required for short-timescale events to be detected with our short-period survey.

We estimate the event rates by using a method based on $1/V_{\rm max}$ method (Schmidt 1968; Eales 1993), which is used for estimation of galaxy luminosity function. The event rates of transients R can be written as $R = \sum_i R_i = \sum_i \frac{1}{p_i \tau_i V_{{\rm max},i}}$. Here, p_i is a detection efficiency ($p_i < 1$), τ_i is the restframe time window for a rapidly rising transient to be detected with our survey, and $V_{{\rm max},i}$ is the maximum volume in which the transient is detectable with our survey. The summation is taken over all the detected objects. The difference from galaxy luminosity function is τ_i in the denominator to take into account the fact that transient event rate should be measured for a given time period. As the number of samples is small, we do not take into account redshift evolution of the event rate.

We do *not* correct detection efficiency since the selection criteria are complicated: we need spectroscopic redshift to define the rapidly rising transients (Section 2.2). Thus, we assume $p_i = 1$, so that the analysis gives a conservative lower limit for the event rate (see below for the possible impact of this assumption).

Then, the free parameter in this analysis is only τ_i. For simplicity, we assume this parameter is the same (τ) for all the objects by neglecting different redshifts. Here, τ means the duration for which transients show a rapid rise with sufficient brightness so that they are recognized as rapidly rising transients in our survey. For the two objects detected on both Days 1 and 2 (SHOOT14or and 14jr), the duration of the emission is about 1.2 days in the observed frame (0.67 and 0.86 days in the restframe, respectively), and thus τ is not much shorter than 1 day. A smaller τ is not excluded for the other three objects but they do not show clear intranight variability for 1.6–3.1 hr in the observed frame (1.0–2.0 hr in the restframe). Comparison with previously known transients (Section 3) and also with models (see Section 5.2) suggests that it is unlikely that the rate of rise as high as $|\Delta m/\Delta t| > 1$ mag day^{-1} continues for >2 days in the restframe with sufficient brightness. Thus, we adopt $\tau = 1$ day as a fiducial value for all objects.

A typical 3σ limiting magnitude for the images used for candidate selection is $\simeq$26.0 mag. We use this value for the calculation of the maximum volume $V_{\rm max}$. In fact, for objects to be recognized as rapidly rising transients, they should be sufficiently brighter than the limiting magnitude on Day 2. Thus, the effective limiting magnitude for the rapidly rising transients tends to be shallower than 26.0 mag. Since analysis with a shallower limiting magnitude gives a smaller maximum volume and a higher event rate, our choice of deep limiting magnitude gives conservative estimates for the event rate. It is noted that the extinction in the host galaxy is not corrected and the true absolute magnitude of our samples should be brighter. However, if the extinction for the current samples represents an average degree of extinction, the estimate of $V_{\rm max}$ is not significantly affected (i.e., our estimate crudely includes the effect of extinction).

We estimate a pseudo event rate for each object (R_i). For example, the maximum redshift at which our survey would have detected SHOOT14gp is $z_{\rm max} = 1.87$, with a limiting magnitude of 26.0 mag using an absolute magnitude of $M = -18.67$ mag and crude K-correction (the term $2.5\log(1+z)$) as in Section 3. The comoving volume within this redshift in the 12 deg^2 survey area is $V_{{\rm max},i} = 0.16$ Gpc^3. For this object to be detected with our survey, the required event rate should be $R_i \simeq 1/\tau_i V_{{\rm max},i} \simeq 0.23 \times 10^{-5} (\tau/1\ {\rm day})^{-1}\ {\rm yr}^{-1}\ {\rm Mpc}^{-3}$. Similar analysis for SHOOT14or, 14 ha, 14jr, and 14ef gives $z_{\rm max} = 1.28$, 0.70, 0.82, and 0.62, and the event rates are $R_i \simeq 0.47,\ 1.9,\ 1.3,\ 2.5\ \times 10^{-5}\ (\tau/1\ {\rm day})^{-1}\ {\rm yr}^{-1}\ {\rm Mpc}^{-3}$, respectively.

By summing up the pseudo rates, the lower limit of the total event rate is $R \simeq 6.4 \times 10^{-5}\ (\tau/1\ {\rm day})^{-1}\ {\rm yr}^{-1}\ {\rm Mpc}^{-3}$. This corresponds to about 9% of the core-collapse SN rate at $z \sim 1$ (the core-collapse SN rate is (3–7) $\times 10^{-4}$ yr^{-1} Mpc^{-3} at $z = 0$–1, Dahlen et al. 2004, 2012; Botticella et al. 2008; Li et al. 2011). Note that the event rate is dominated by less luminous objects with smaller maximum volumes. The event rate for the two luminous events (SHOOT14gp and 14or) is $R = 0.7 \times 10^{-5}\ (\tau/1\ {\rm day})^{-1}\ {\rm yr}^{-1}\ {\rm Mpc}^{-3}$ (~1% of the core-collapse SN rate at $z \sim 1$), while that for the three faint events (SHOOT14ha, 14jr, and 14ef) is $R = 5.7 \times 10^{-5}\ (\tau/1\ {\rm day})^{-1}\ {\rm yr}^{-1}\ {\rm Mpc}^{-3}$ (~8% of the core-collapse SN rate). It is worth mentioning that the event rate of the rapid transients from PS1 is estimated to be 4%–7% of the core-collapse SN

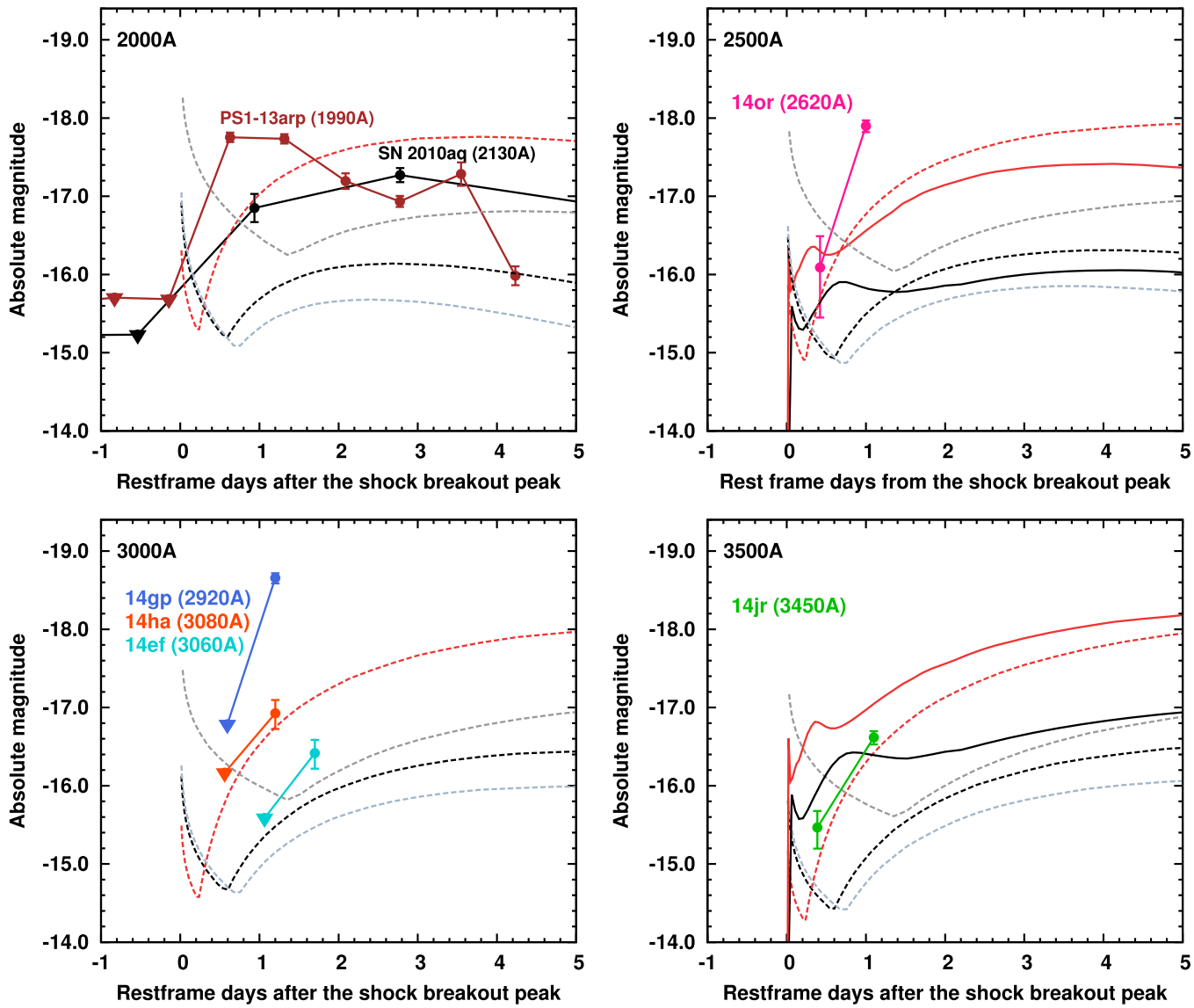

Figure 10. Comparison between the observed light curves and model light curves. The dashed lines show analytic model light curves of cooling envelope emission for red supergiant SNe from Nakar & Sari (2010): black ($M_{\rm ej}$, R, E) = (15 $M_\odot$, 500 $R_\odot$, 1.0 × 10^{51} erg), upper gray (15 $M_\odot$, 1000 $R_\odot$, 1.0 × 10^{51} erg), lower gray (25 $M_\odot$, 500 $R_\odot$, 1.0 × 10^{51} erg), and red (15 $M_\odot$, 500 $R_\odot$, 5.0 × 10^{51} erg). The black and red solid lines in the panels for 2500 and 3500 Å are numerical models calculated with *STELLA*: ($M_{\rm ej}$, R, E) = (15 $M_\odot$, 500 $R_\odot$, 1.2 × 10^{51} erg) and (15 $M_\odot$, 500 $R_\odot$, 4.0 × 10^{51} erg), respectively. Epochs of observed data are arbitrarily shifted to match the models.

rate (Drout et al. 2014), which is broadly consistent with our estimate.

As described above, our estimate involves crude approximation, mainly due to (1) incompleteness of the sample, (2) a choice of a simple magnitude limit, and (3) unknown transient duration. To anchor a possible range of uncertainties, we here discuss the impacts of each effect. (1) As discussed in Section 2.2, we could not take spectra of six SN candidates. If all of them satisfy the criteria of rapid transients, the total number of objects is 11 instead of 5. The actual impact on the event rate depends on their luminosity and redshifts, but if all of them are assumed to be similar to our faint samples (with a high event rate), the total event rate can be increased at most by a factor of about 2.2 (11/5). (2) If a shallow magnitude limit is adopted, it results in a smaller $V_{\rm max}$ and a higher event rate. By adopting a limit of 25.5 mag, which is the shallowest possible limit to detect SHOOT14ef, the event rate is increased by a factor of 1.7. (3) The effect of duration (τ) is crudely expressed in a term of τ^{-1} and it can either reduce or increase the event rate. The event rate is reduced by a factor of 2 for the duration of $\tau = 2$ days, while it is increased by a factor of 1.4 for the duration of $\tau = 0.7$ days (SHOOT14or).

In summary, our estimate of rate is uncertain by a factor of ∼2 for reduction and ∼5 for increase. In either case, the event rate is not totally negligible compared with the core-collapse SN rate. Given the crude approximation in the estimate, the true event rate can be comparable to the SN rate, i.e., the rapidly rising phase can be associated with all core-collapse SNe.

5.2. Nature of the Rapidly Rising Transients

Shock breakout. The electromagnetic signal from SNe starts with shock breakout emission. Shock breakout occurs when the diffusion timescale of photons in front of the shock wave

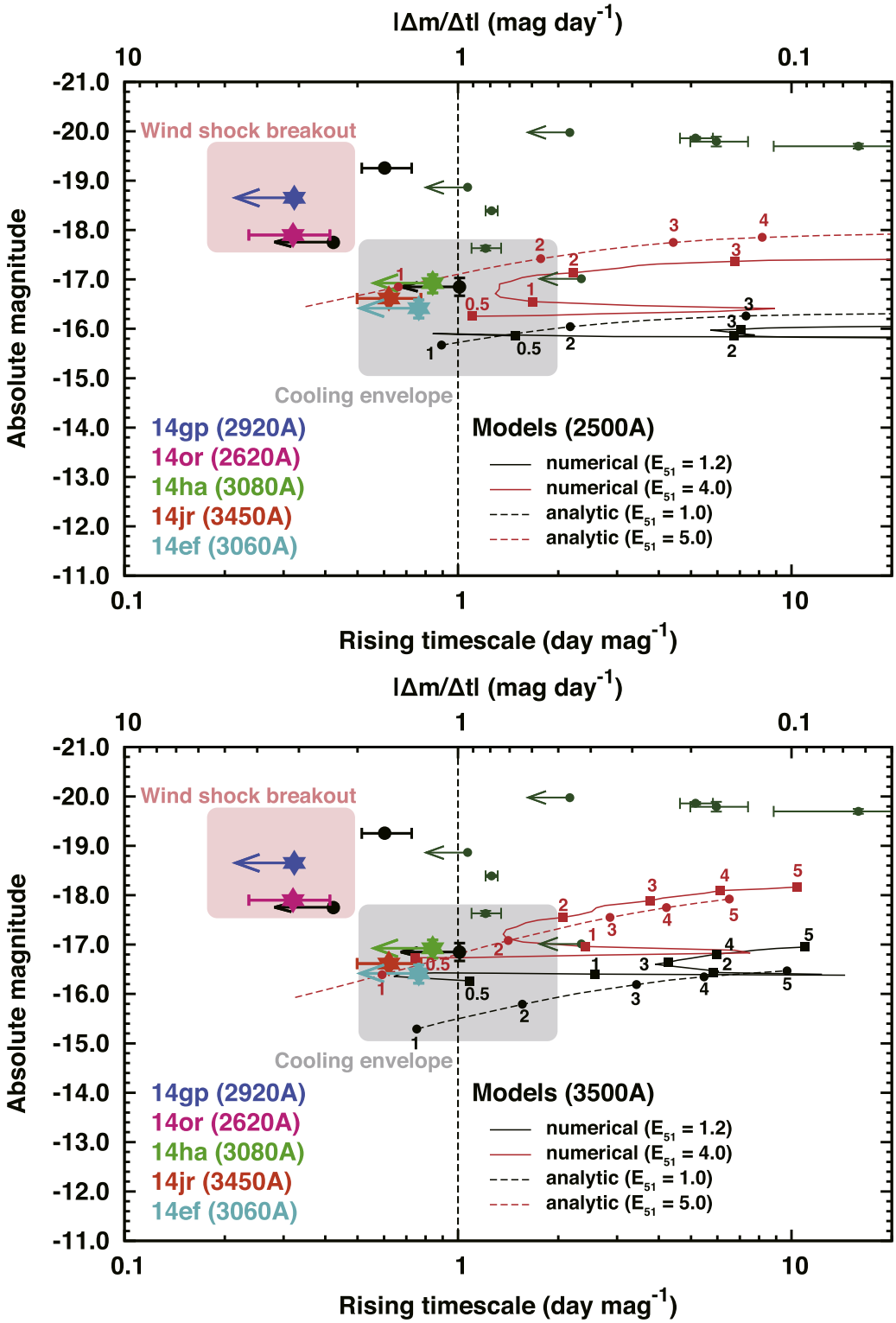

Figure 11. Absolute magnitude and rising timescale (as in Figure 9) compared with analytic and numerical models of the explosion of a red supergiant. Upper and lower panels show the models at 2500 Å and 3500 Å respectively. The solid and dashed lines show numerical and analytic models, respectively. The parameters of the models are the following. Numerical models: black solid ($M_{\rm ej}$, R, E) = (15 $M_\odot$, 500 $R_\odot$, 1.2 × 10^{51} erg) and red solid (15 $M_\odot$, 500 $R_\odot$, 4.0 × 10^{51} erg). Analytic models: black dashed ($M_{\rm ej}$, R, E) = (15 $M_\odot$, 500 $R_\odot$, 1.0 × 10^{51} erg) and red dashed (15 $M_\odot$, 500 $R_\odot$, 5.0 × 10^{51} erg). The time evolution of the models is connected with lines. Numbers associated with dots show the epochs (in days) from the peak of the shock breakout.

becomes as short as the dynamical timescale (Falk 1978; Klein & Chevalier 1978). A typical duration of shock breakout at the stellar surface is the light crossing time of the progenitor size, i.e., ∼1000 s for a red supergiant progenitor of 500 $R_\odot$ (e.g., Ensman & Burrows 1992; Matzner & McKee 1999; Tominaga et al. 2009, 2011) and shorter for more compact progenitors.

The observed timescale for SHOOT14or and 14jr, which are detected on both Days 1 and 2 (0.55–0.72 days in restframe), is

much longer than the expected timescales of shock breakout emission. Therefore, they cannot be shock breakout emission at the stellar surface. On the other hand, the other three objects (SHOOT14gp, 14 ha, and 14ef) are not detected on Day 1, and thus the possibility of shock breakout is not ruled out. However, they do not show significant intranight variability within 1.0, 1.1, and 2.0 hr (restframe) on Day 2, respectively, and interpretation as shock breakout is not necessarily required for these three objects.

Cooling envelope emission. Following shock breakout emission, SNe show emission from the cooling envelope (Waxman et al. 2007; Chevalier & Fransson 2008; Nakar & Sari 2010; Rabinak & Waxman 2011). This phase is believed to have been detected for SNe with very early detection, such as SNe 2006aj and 2008D (Waxman et al. 2007; Chevalier & Fransson 2008; Soderberg et al. 2008; Modjaz et al. 2009; Nakar 2015, but see Bersten et al. 2013 for caveats on SN 2008D). The early UV detection of SN 2010aq (Figure 6) is also interpreted as cooling emission (Gezari et al. 2010). Drout et al. (2014) also showed that, among their rapid transients from PS1, the faint objects such as PS1-10ah can be interpreted as cooling envelope emission. In addition to these very early detections, the tail of the cooling phase is sometimes observed in some other SNe, such as SNe 1993J, 1999ex, and 2011dh, at later phases (e.g., Lewis et al. 1994; Richmond et al. 1994; Stritzinger et al. 2002; Arcavi et al. 2011; Marion et al. 2014).

Figure 10 shows light curves of cooling envelope emission for red supergiant cases from Nakar & Sari (2010), compared with light curves of our samples, SN 2010aq, and PS1-13arp. We divide these objects into four classes according to effective restframe wavelength (2000, 2500, 3000, and 3500 Å). The black dashed lines show the fiducial model with the ejecta mass $M_{\rm ej} = 15\,M_\odot$, progenitor radius $R = 500\,R_\odot$, and explosion energy $E = 1.0 \times 10^{51}$ erg. Other lines show models with different mass, radius, and energy: upper gray dashed line ($M_{\rm ej}$, R, E) = (15 $M_\odot$, 1000 $R_\odot$, 1.0×10^{51} erg), lower gray dashed (25 $M_\odot$, 500 $R_\odot$, 1.0×10^{51} erg), and red dashed (15 $M_\odot$, 500 $R_\odot$, 5.0×10^{51} erg). The epochs of observed data are arbitrarily shifted to match the models. The brightness of observed samples is consistent with or brighter than the red supergiant models. Since the cooling envelope emission from explosions of more compact progenitors tends to be fainter than the red supergiant case in UV at ∼1 day (Nakar & Sari 2010), models with blue supergiant or Wolf–Rayet star progenitors do not give better agreement.

The light curve of SHOOT14jr is qualitatively consistent with a model of cooling envelope emission. SHOOT14ha and 14ef can also be explained by the models, although they are detected only on Day 2. Since the cooling envelope emission peaks at an epoch when $h\nu \sim 3kT$ is fulfilled, the spectral peak at the rising phase is located at shorter wavelengths than the observed wavelengths. This is also consistent with the blue color of our objects. Note that comparison with the models suggests an explosion energy higher than 1.0×10^{51} erg. In addition, due to possible extinction in the host galaxies, the true absolute magnitudes of our objects can be even brighter. These situations are also the case for SN 2010aq, where a model brighter than our fiducial model by 1.5 mag gives the best match with the observed data without correction for host extinction (Gezari et al. 2010).

To understand possible varieties in the models, we also show selected numerical models for the early phase of SNe IIP. The models are calculated with the multigroup radiation hydrodynamics code *STELLA* (Blinnikov et al. 2006). For the purpose of parametric studies, quasi-polytrope pre-SN models are constructed in hydrostatic equilibrium by assuming the solar metallicity and a power-law dependence of the temperature on the density as in Baklanov et al. (2005, 2015). In Figure 10, magnitudes in *Swift uvw*1- and *u*-filters are shown in the panels for 2500 and 3500 Å data. Black and red solid lines show the models with similar parameters to those for analytic models: ($M_{\rm ej}$, R, E) = (15 $M_\odot$, 500 $R_\odot$, 1.2×10^{51} erg) and (15 $M_\odot$, 500 $R_\odot$, 4.0×10^{51} erg), respectively. Although there are some discrepancies between analytic and numerical models, the trend is similar: SHOOT14jr can be consistent with models while SHOOT14or is brighter and faster than the models.

Figure 11 shows the rising timescales and absolute magnitudes (as in Figure 9) compared with those of analytic (dashed) and numerical (solid) models. The black and red lines show the fiducial models and models with a higher energy. As also shown in Figure 10, the model light curves are consistent with the three faint objects in our samples at $\lesssim$1–2 days after the shock breakout.

In summary, the three faint objects (SHOOT14ha, 14jr, and 14ef) out of our five samples are interpreted to be the cooling envelope emission from the explosion of a red supergiant. The epoch of our detection is likely to be $\lesssim$1–2 days after the shock breakout.

Shock breakout from a dense wind. SHOOT14gp and SHOOT14or, two luminous objects in our samples, are brighter and faster than the cooling envelope models. In fact, this difficulty is also found for the cases of PTF 09uj and PS1-13arp. Ofek et al. (2010) and Gezari et al. (2015) interpreted the emission as shock breakout from a dense wind since that can be more luminous than cooling envelope emission by a factor of $\gtrsim$10 (Ofek et al. 2010; Balberg & Loeb 2011; Chevalier & Irwin 2011; Moriya et al. 2011).

For the shock breakout from the wind, the timescale to the peak luminosity reflects the diffusion timescale in the wind, $t_p = 6.6(\kappa/0.34\,{\rm cm^2\,g^{-1}})(\dot{M}/10^{-2}\,M_\odot\,{\rm yr^{-1}})\quad(v_{\rm wind}/10\,{\rm km\,s^{-1}})$ days (Chevalier & Irwin 2011), where $\dot{M}$ and $v_{\rm wind}$ are the mass loss rate and wind velocity, respectively. For our samples, the time to the peak is not tightly constrained, but it is longer than 0.55 days for SHOOT14or. Therefore, the required mass loss rate is of the order of $10^{-3} M_\odot$ yr^{-1} for a wind velocity of $v_{\rm wind} = 10$ km s^{-1}. A typical epoch when such a mass loss rate is required is $t_{\rm wind} \sim 2.7(v_{\rm SN}/10{,}000\,{\rm km\,s^{-1}})(v_{\rm wind}/10\,{\rm km\,s^{-1}})^{-1}(t_{\rm SN}/1\,{\rm day})$ years before the explosion, where $v_{\rm SN}$ and $t_{\rm SN}$ are the shock velocity of the SN and the observed time after explosion, respectively.

The inferred mass loss rate is higher than that typically estimated for red supergiants, $\dot{M} \lesssim 10^{-4}\,M_\odot$ yr^{-1} (van Loon et al. 2005; Mauron & Josselin 2011), and as high as the enhanced, episodic mass loss rate estimated for VY Canis Majoris ((1–2) $\times 10^{-3}\,M_\odot$ yr^{-1}, Smith et al. 2009). If our interpretation is the case, our study implies that $\gtrsim$1% of massive stars can have such a high mass loss rate at the very end of their evolution (i.e., a few years before the explosion).

Drout et al. (2014) also suggested that the PS1 luminous samples are the shock breakout from the wind. The PS1 luminous samples show a longer timescale than those for our two luminous samples and PS1-13arp (Figure 9). This may be understood as the different mass loss rates of the wind: the PS1

luminous samples require a higher mass loss rate of $\sim 10^{-2} M_{\odot}$ yr^{-1} (Drout et al. 2014).

6. CONCLUSIONS

We perform a high-cadence transient survey using Subaru/HSC. In observations made on two consecutive nights, we detected five rapidly rising transients at $z = 0.384$–0.821 with a rate of rise faster than 1 mag per day in the restframe ($|\Delta m/\Delta t| > 1$ mag day^{-1}). The absolute magnitudes of the five objects range from -16 to -19 mag in the restframe near-UV wavelengths, and they all show blue colors, $g - r \lesssim -0.2$ mag.

To our knowledge, the rates of rise and brightness of our samples are most similar to those of the very early phase (< a few days after the explosion) of core-collapse SNe, such as SN 2010aq and PS1-13arp detected by *GALEX* in the very early phases (Gezari et al. 2010, 2015), and the faint population of rapid transients from PS1 (Drout et al. 2014). A conservative estimate suggests that the event rate of rapidly rising transients is $\gtrsim$9% of core-collapse SN rates, assuming a typical duration of the fast rising phase in the near-UV wavelengths to be 1 day. The true event rate can be comparable to the core-collapse SN rate.

Although spectroscopic identification is not available, the rapidly rising transients presented in this paper are interpreted to be the very early phase of core-collapse SNe. The observed light curves of three faint objects (SHOOT14ha, 14jr, and 14ef) are qualitatively consistent with the cooling envelope emission from the explosion of red supergiants. Comparison with analytic and numerical models shows that the epochs of our observations correspond to $\lesssim$1–2 days after the shock breakout.

The other two luminous objects (SHOOT14gp and 14or) are brighter and faster than the expectation of the cooling envelope models. We interpret them as shock breakout emission from a dense wind, as also suggested for PS1-13arp. The required mass loss rate is $\sim 10^{-3} M_{\odot}$ yr^{-1}. The event rate of these luminous events is higher than $\sim$1% of the core-collapse SN rate. Therefore, if our interpretation is correct, it implies that more than $\sim$1% of massive stars can experience such a strong mass loss a few years before the explosion.

We thank the anonymous referee for constructive comments that improved the paper. This research was in part supported by Grants-in-Aid for Scientific Research of JSPS (23224004, 23740157, 24740117, 25800103, 26400222, 15H02075, 15H05440), MEXT (25103515, 15H00788), the World Premier International Research Center Initiative, MEXT, Japan, the research grant program of Toyota foundation (D11-R-0830), and the RFBR-JSPS bilateral program. S.B. and P.B. are supported in the work on *STELLA* code by the Russian Science Foundation Grant No. 14-12-00203. T.J.M. is supported by JSPS Postdoctoral Fellowships for Research Abroad (26·51). Support for H.K. is provided by the Ministry of Economy, Development, and Tourism's Millennium Science Initiative through grant IC120009, awarded to The Millennium Institute of Astrophysics, MAS. H.K. acknowledges support by CONICYT through FONDECYT grant 3140563. This paper makes use of software developed for the LSST. We thank the LSST Project for making their code available as free software at http://dm.lsstcorp.org.

REFERENCES

Aihara, H., Allende Prieto, C., An, D., et al. 2011, ApJS, 193, 29
Alard, C. 2000, A&AS, 144, 363
Alard, C., & Lupton, R. H. 1998, ApJ, 503, 325
Arcavi, I., Gal-Yam, A., Yaron, O., et al. 2011, ApJL, 742, L18
Arcavi, I., Wolf, W. M., Howell, D. A., et al. 2015, arXiv:1511.00704
Axelrod, T., Kantor, J., Lupton, R. H., & Pierfederici, F. 2010, Proc. SPIE, 7740, 15
Bailey, S., Aragon, C., Romano, R., et al. 2007, ApJ, 665, 1246
Baklanov, P. V., Blinnikov, S. I., & Pavlyuk, N. N. 2005, AstL, 31, 429
Baklanov, P. V., Sorokina, E. I., & Blinnikov, S. I. 2015, AstL, 41, 95
Balberg, S., & Loeb, A. 2011, MNRAS, 414, 1715
Becker, A. C., Wittman, D. M., Boeshaar, P. C., et al. 2004, ApJ, 611, 418
Berger, E., Leibler, C. N., Chornock, R., et al. 2013, ApJ, 779, 18
Bersten, M. C., Tanaka, M., Tominaga, N., Benvenuto, O. G., & Nomoto, K. 2013, ApJ, 767, 143
Blinnikov, S. I., Röpke, F. K., Sorokina, E. I., et al. 2006, A&A, 453, 229
Bloom, J. S., Richards, J. W., Nugent, P. E., et al. 2012, PASP, 124, 1175
Botticella, M. T., Riello, M., Cappellaro, E., et al. 2008, A&A, 479, 49
Breeveld, A. A., Landsman, W., Holland, S. T., et al. 2011, in AIP Conf. Proc. 1358, Gamma Ray Bursts 2010, ed. J. E. McEnery, J. L. Racusin, & N. Gehrels (Melville, NY: AIP), 373
Brink, H., Richards, J. W., Poznanski, D., et al. 2013, MNRAS, 435, 1047
Brown, P. J., Dawson, K. S., de Pasquale, M., et al. 2012, ApJ, 753, 22
Brown, P. J., Roming, P. W. A., Milne, P., et al. 2010, ApJ, 721, 1608
Campana, S., Mangano, V., Blustin, A. J., et al. 2006, Natur, 442, 1008
Chevalier, R. A., & Fransson, C. 2008, ApJL, 683, L135
Chevalier, R. A., & Irwin, C. M. 2011, ApJL, 729, L6+
Chomiuk, L., Chornock, R., Soderberg, A. M., et al. 2011, ApJ, 743, 114
Dahlen, T., Strolger, L.-G., Riess, A. G., et al. 2012, ApJ, 757, 70
Dahlen, T., Strolger, L.-G., Riess, A. G., et al. 2004, ApJ, 613, 189
Drake, A. J., Djorgovski, S. G., Mahabal, A., et al. 2009, ApJ, 696, 870
Drout, M. R., Chornock, R., Soderberg, A. M., et al. 2014, ApJ, 794, 23
Drout, M. R., Soderberg, A. M., Mazzali, P. A., et al. 2013, ApJ, 774, 58
Eales, S. 1993, ApJ, 404, 51
Ensman, L., & Burrows, A. 1992, ApJ, 393, 742
Falk, S. W. 1978, ApJL, 225, L133
Flaugher, B., Diehl, H. T., Honscheid, K., et al. 2015, AJ, 150, 150
Forster, F., Maureira, J. C., Gonzalez-Gaitan, S., & Galbany, L. 2014, ATel, 5949, 1
Furusawa, H., Okura, Y., Mineo, S., et al. 2011, PASJ, 63, 585
Gall, E. E. E., Polshaw, J., Kotak, R., et al. 2015, A&A, 582, 83
Gal-Yam, A. 2012, Sci, 337, 927
Gal-Yam, A., Arcavi, I., Ofek, E. O., et al. 2014, Natur, 509, 471
Ganot, N., Gal-Yam, A., Ofek, E. O., et al. 2014, arXiv:1412.4063
Gezari, S., Jones, D. O., Sanders, N. E., et al. 2015, ApJ, 804, 28
Gezari, S., Rest, A., Huber, M. E., et al. 2010, ApJL, 720, L77
González-Gaitán, S., Tominaga, N., Molina, J., et al. 2015, MNRAS, 451, 2212
Hogg, D. W., Baldry, I. K., Blanton, M. R., & Eisenstein, D. J. 2002, arXiv: astro-ph/0210394
Ivezic, Z., Tyson, J. A., Abel, B., et al. 2008, arXiv:0805.2366
Kaiser, N., Burgett, W., Chambers, K., et al. 2010, Proc. SPIE, 7733, 77330E
Kashikawa, N., Aoki, K., Asai, R., et al. 2002, PASJ, 54, 819
Kashiyama, K., & Quataert, E. 2015, MNRAS, 451, 2656
Kasliwal, M. M. 2012, PASA, 29, 482
Kasliwal, M. M., Kulkarni, S. R., Gal-Yam, A., et al. 2010, ApJL, 723, L98
Klein, R. I., & Chevalier, R. A. 1978, ApJL, 223, L109
Komatsu, E., Dunkley, J., Nolta, M. R., et al. 2009, ApJS, 180, 330
Law, N. M., Kulkarni, S. R., Dekany, R. G., et al. 2009, PASP, 121, 1395
Lewis, J. R., Walton, N. A., Meikle, W. P. S., et al. 1994, MNRAS, 266, L27
Li, W., Leaman, J., Chornock, R., et al. 2011, MNRAS, 412, 1441
LSST Science Collaboration 2009, arXiv:0912.0201
Marion, G. H., Vinko, J., Kirshner, R. P., et al. 2014, ApJ, 781, 69
Matzner, C. D., & McKee, C. F. 1999, ApJ, 510, 379
Mauron, N., & Josselin, E. 2011, A&A, 526, A156
Mazzali, P. A., Deng, J., Pian, E., et al. 2006, ApJ, 645, 1323
Mazzali, P. A., Valenti, S., Della Valle, M., et al. 2008, Sci, 321, 1185
Metzger, B. D., Piro, A. L., & Quataert, E. 2009, MNRAS, 396, 1659
Mirabal, N., Halpern, J. P., An, D., Thorstensen, J. R., & Terndrup, D. M. 2006, ApJL, 643, L99
Miyazaki, S., Komiyama, Y., Nakaya, H., et al. 2006, Proc. SPIE, 6269, 62690B
Miyazaki, S., Komiyama, Y., Nakaya, H., et al. 2012, Proc. SPIE, 8446, 84460Z

Modjaz, M., Stanek, K. Z., Garnavich, P. M., et al. 2006, ApJL, 645, L21
Modjaz, M., Li, W., Butler, N., et al. 2009, ApJ, 702, 226
Moriya, T., Tominaga, N., Blinnikov, S. I., Baklanov, P. V., & Sorokina, E. I. 2011, MNRAS, 415, 199
Morokuma, T., Tominaga, N., Tanaka, M., et al. 2014, PASJ, 66, 114
Nakar, E. 2015, ApJ, 807, 172
Nakar, E., & Sari, R. 2010, ApJ, 725, 904
Nugent, P. E., Sullivan, M., Cenko, S. B., et al. 2011, Natur, 480, 344
Ofek, E. O., Rabinak, I., Neill, J. D., et al. 2010, ApJ, 724, 1396
Pastorello, A., Cappellaro, E., Inserra, C., et al. 2013, ApJ, 767, 1
Pastorello, A., Smartt, S. J., Botticella, M. T., et al. 2010, ApJL, 724, L16
Pian, E., Mazzali, P. A., Masetti, N., et al. 2006, Natur, 442, 1011
Poznanski, D., Chornock, R., Nugent, P. E., et al. 2010, Sci, 327, 58
Prieto, J. L., Brimacombe, J., Drake, A. J., & Howerton, S. 2013, ApJL, 763, L27
Pritchard, T. A., Roming, P. W. A., Brown, P. J., Bayless, A. J., & Frey, L. H. 2014, ApJ, 787, 157
Quimby, R. M., Kulkarni, S. R., Kasliwal, M. M., et al. 2011, Natur, 474, 487
Quimby, R. M., Wheeler, J. C., Höflich, P., et al. 2007, ApJ, 666, 1093
Rabinak, I., & Waxman, E. 2011, ApJ, 728, 63
Rau, A., Kulkarni, S. R., Law, N. M., et al. 2009, PASP, 121, 1334
Rau, A., Ofek, E. O., Kulkarni, S. R., et al. 2008, ApJ, 682, 1205
Richmond, M. W., Treffers, R. R., Filippenko, A. V., et al. 1994, AJ, 107, 1022
Rubin, A., Gal-Yam, A., De Cia, A., et al. 2015, arXiv:1512.00733
Sako, S., Aoki, T., Doi, M., et al. 2012, Proc. SPIE, 8446, 84466L
Schmidt, M. 1968, ApJ, 151, 393
Šimon, V., Pizzichini, G., & Hudec, R. 2010, A&A, 523, A56
Smith, N., Hinkle, K. H., & Ryde, N. 2009, AJ, 137, 3558
Soderberg, A. M., Berger, E., Page, K. L., et al. 2008, Natur, 453, 469
Soderberg, A. M., Kulkarni, S. R., Nakar, E., et al. 2006, Natur, 442, 1014
Sollerman, J., Jaunsen, A. O., Fynbo, J. P. U., et al. 2006, A&A, 454, 503
Stritzinger, M., Hamuy, M., Suntzeff, N. B., et al. 2002, AJ, 124, 2100
Tanaka, M., Morokuma, T., Itoh, R., et al. 2014, ApJL, 793, L26
Tanaka, M., Tominaga, N., Nomoto, K., et al. 2009a, ApJ, 692, 1131
Tanaka, M., Yamanaka, M., Maeda, K., et al. 2009b, ApJ, 700, 1680
Tominaga, N., Blinnikov, S., Baklanov, P., et al. 2009, ApJL, 705, L10
Tominaga, N., Morokuma, T., Blinnikov, S. I., et al. 2011, ApJS, 193, 20
Tominaga, N., Morokuma, T., Tanaka, M., et al. 2014a, ATel, 6291, 1
Tominaga, N., Morokuma, T., Tanaka, M., et al. 2014b, ATel, 6763, 1
Tominaga, N., Morokuma, T., Tanaka, M., et al. 2015a, ApJ, submitted
Tominaga, N., Morokuma, T., Tanaka, M., et al. 2015b, ATel, 7565, 1
Tominaga, N., Morokuma, T., Tanaka, M., et al. 2015c, ATel, 7927, 1
van Loon, J. T., Cioni, M.-R. L., Zijlstra, A. A., & Loup, C. 2005, A&A, 438, 273
Waxman, E., Mészáros, P., & Campana, S. 2007, ApJ, 667, 351
Yamanaka, M., Maeda, K., Kawabata, M., et al. 2014, ApJL, 782, L35